Dense, Vertical Gas-Solid Flow in a Pipe

Aubrey Miller and Dimitri Gidaspow
Dept. of Chemical Engineering, Illinois Institute of Technology, Chicago, IL 60616

The hydrodynamics of gas-solid flow, usually referred to as circulating fluidized-bed flow, was studied in a 7.5-cm clear acrylic riser with 75-μm FCC catalyst particles. Data were obtained for three central sections as a function of gas and solids flow rates. Fluxes were measured by means of an extraction probe. Particle concentrations were measured with an X-ray densitometer. In agreement with previous investigators, these data showed the flow to be in the core-annular regime, with a dilute rising core and a dense descending annular region. However, unlike the previous studies conducted worldwide, the data obtained in this investigation allowed us to determine the viscosity of the suspension. The viscosity was a linear function of the volume fraction of solids. It extrapolates to the high bubbling-bed viscosities.

Introduction

This study is part of a worldwide effort to understand the hydrodynamics of dense vertical gas-solid flow in a pipe usually referred to in the literature as circulating fluidized bed or riser flow: from Canada, Grace et al. (1990); from China, Kwauk et al. (1986); from England, Rhodes et al. (1989); from Finland, Engstrom (1990); from France, Galtier et al. (1989); and from the U.S., Bader et al. (1988), Louge et al. (1991), and Weinstein et al. (1986). Earlier it was called fast fluidization (Squires et al., 1985; Yerushalmi, 1986). The motivation for this effort comes from the following two technologies. In the oil industry, the development of more active catalysts for the production of gasoline requires a replacement of the older bubbling beds with circulating fluidized bed units. In the electric power production industry, the new standards require that coal be burned with much lower emissions of sulfur and nitrogen oxides. Circulating fluidized-bed combustors containing adsorbents such as limestone appear to be ideally suited for the production of clean energy from high-sulfur coals. Unfortunately, earlier attempts to use bubbling fluidized beds with internal heat exchange tubes were not successful due to severe tube erosion problems which were not known before the construction of large pilot and demonstration plants. Such past failures require that the hydrodynamics of dense flow be better understood.

Earlier dense flow hydrodynamic studies measured either only the solid velocities (Tsuji, 1984) or the particle concentrations (Weinstein et al. 1986). At several recent National Science Foundation and U.S. Department of Energy meetings, it was recognized and agreed that minimum understanding of two-phase flow requires the simultaneous measurement of both the particle velocity and its concentration as a function of position. Bader et al.'s (1988) study appears to be the first in which both the radial particle velocities and the radial concentrations were determined for riser flow. Such data are needed to compare them to the theoretical models of gas-particle flow. For example, Sinclair and Jackson (1989) used a granular kinetic theory model developed by Savage and collaborators (1983) to describe the fully-developed steady-state flow regimes in a riser. Hence, there is a need for experimental studies of riser flow.

The radial velocity and concentration distributions obtained in this study permit us to obtain the effective solids viscosity as a function of particle concentration. Tsuo and Gidaspow (1990) used such estimated viscosities to obtain the two flow regimes observed in the riser: the core-annular regime studied here and the more dilute cluster regime observed with larger, Geldart group B particles. Calculations for the core annular regime are strikingly similar to the data presented in this article. In the core the velocity of the particles is as much as twice the superficial gas velocity. The annular region is dense and flows down slowly. The downflow disappears at a sufficiently high gas velocity. The system never reaches a true steady state, but oscillates slowly. The particles running down at the wall observed in this study using a video camera oscillate in the manner computed for a complete loop using a new version of the kinetic theory (Gidaspow et al., 1992). A workshop on riser hydrodynamics held in May 1992 in Broadbeach, Australia at the 7th International Fluidization Conference (Potter and Nicklin, 1992) showed that there was a general agreement concerning the shape of the density and velocity profiles reported here.

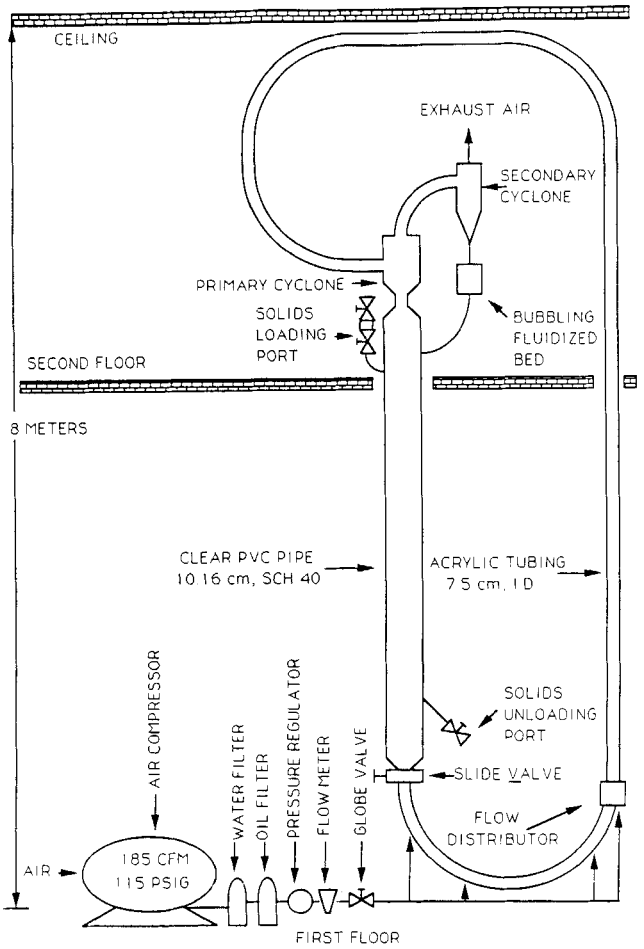

Figure 1. Circulating fluidized bed.

Experimental Equipment

Circulating fluidized bed

A cold-model, circulating, fluidized-bed (CFB) test unit has been constructed at IIT, as shown in Figure 1. Air enters the CFB in its bottom U section along with FCC catalyst particles. The air/catalyst mixture flows from the U through a flow distributor with 38.1-mm-ID, schedule 40 nozzle that distributes the flow semisymmetrically into a 7.5-cm-ID clear acrylic riser, which is approximately 6.58-m-long and is fabricated in four removable sections. To reduce exit effects the mixture flows from the riser through a series of elbows and straight, clear PVC pipe. The piping has an ID of 7.5 cm and the elbows have a centerline radius of 45.72 cm which is identical to that of the U. The effluent stream enters the primary cyclone where separation of gas and particles takes place. To facilitate high solids loadings, the dust outlet of the cyclone has a wide mouth and opens directly to the storage column. Additional separation is obtained in the smaller, more efficient, secondary cyclone. The upflow of air through the bottom of the secondary cyclone must be limited to maintain its separation efficiency. To accomplish this objective, the solids discharge of the cyclone is immersed in a bubbling fluidized bed. The cyclone is positioned at sufficient height above the bed to provide adequate static head for sufficient solids flow. This prevents the accumulation of particles in the cyclone cone. Solids overflow from the bubbling bed to the unfluidized storage hopper. The storage hopper is fabricated of clear 10.16-cm, schedule 40 PVC, which is approximately 4.75 m in length. Solids loading and unloading ports are installed on the top and bottom of the hopper, respectively. The double ball valve layout of the solids loading port and single ball valve arrangement of the unloading port allows the loading and unloading of solids during CFB operation. Catalyst flows from the hopper through a slide valve, which is used to control the solids flow to the downstream U. The solids flow is metered by injecting colored tracer particles into the hopper. The solids flow rate is determined by measuring the rate of descent of the colored particles through the clear PVC pipe with a ruler and stopwatch, assuming plug flow. This assumption has been shown to be very reliable by extracting solids at similar flow rates through the solids unloading port and comparing the extracted amount of solids to that predicted with the tracer particles. A supplementary method of maintaining the same solids flow rate between different operations of the CFB was to adjust the slide valve until the riser pressure drop was similar to the pressure drop of the previous operation.

X-Ray Densitometer

Equipment

Radial solids volume fraction profiles were obtained with an X-ray densitometer. A schematic drawing of the device is shown in Figure 2. The probe contains a 200-mCi Curium 244 source centered at the capped-off outlet of a 2.54-cm, sch 40, steel pipe. The cap of the pipe is covered with 1.27-cm-thick lead to prevent X-ray scatter. A 0.635-cm-OD tube, which is approximately 15-cm-long, extends from the X-ray source, through the lead to the CFB. It is capped off to prevent particles from flowing into it. The tube extends through a male run tee into the CFB. Plastic ferrules are used in the tee so that the tube may be continuously repositioned. When positioning the tube, air is continuously purged through the tee to prevent the binding of the instrument and the escape of particulate.

A colinear X-ray beam flows from the tip of the X-ray probe through the absorbing material (FCC catalyst particles and gas stream) and CFB acrylic pipe to a thallium-activated, sodium iodide scintillation detector where the X-rays are absorbed. A pre-amplifier and an amplifier are used to amplify the detector output pulse to potentials high enough to pass through the window of a pulse-height selector. The window of the selector is set as narrow as possible to eliminate noise that may distort the final count rate. Output from the selector is fed to a counter and timer that provides readout and display of the X-ray intensity data in an accumulative digital mode over a selected time interval.

Calculation of the solid volume fraction from data

The Beer-Lambert law is the mathematical basis used to analyze the experimental data. For the air-solids mixture analyzed in this work, the solid volume fraction (ϵ_s) is calculated in accordance with the following expression (Miller, 1991):

$$\epsilon_s = \frac{\left(\frac{\partial \ln I}{\partial t} + v_a \rho_a\right)}{(v_a \rho_a - v_s \rho_s)} \tag{1}$$

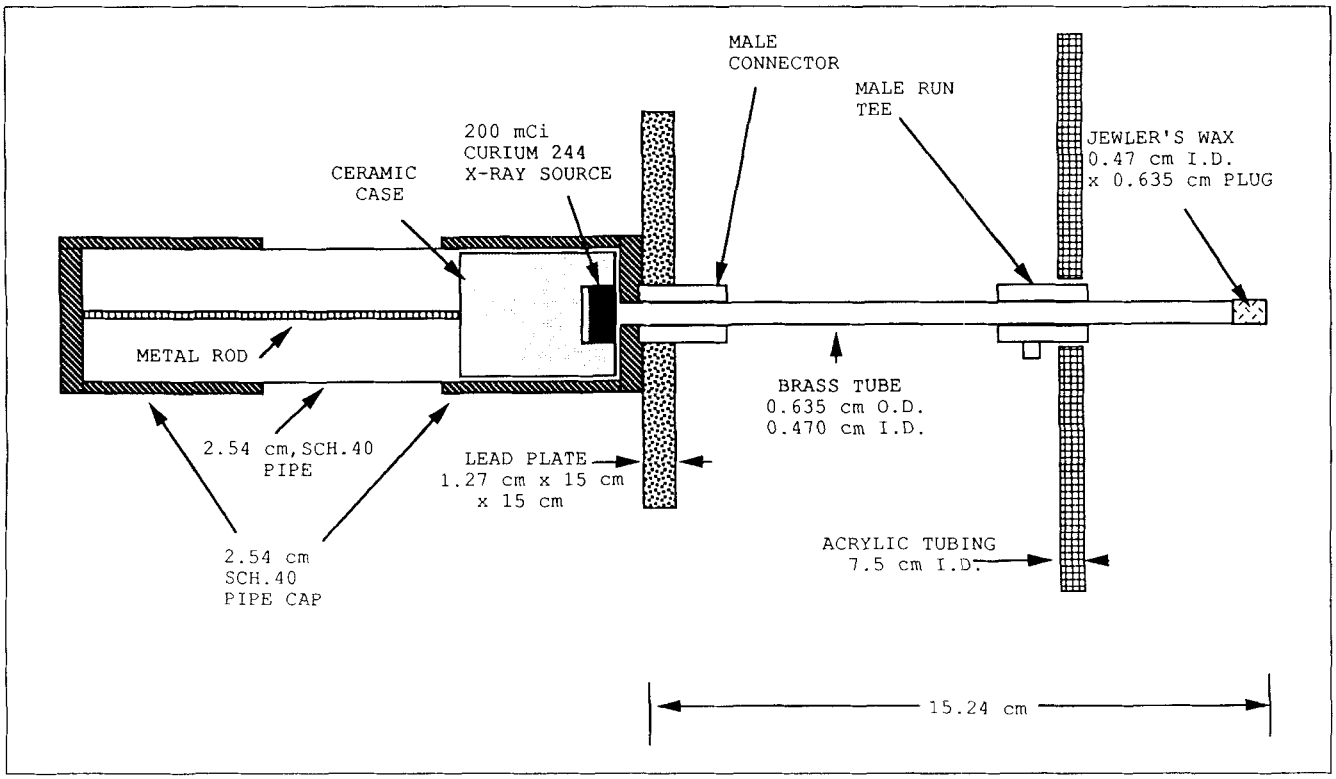

Figure 2. X-ray densitometer.

The solid volume fraction (ϵ_s) is calculated directly from a plot of the natural logarithm of intensity vs. distance, since all other components of the equation are constant.

For each solid volume fraction profile, intensity measurements were obtained across the diameter of the riser. All intensity measurements were time-averaged over a 10-minute interval to minimize unsteady-state effects. The tip of the extraction probe's 0.635-cm-dia. tube was first placed adjacent to the far riser wall (next to the scintillation counter). The value of the intensity measured at this point was taken as I_0. The probe was then moved away from the wall in 0.635 cm increments, taking an intensity measurement at each point until an intensity profile was obtained for the entire riser diameter.

The natural logarithm of intensity vs. radial distance is plotted in Figure 3 for relatively dilute operating conditions. At the far wall (radial span 0.0 to 0.635 cm), the intensity drops sharply. Over the radial span 0.635 to 5.08 cm, the intensity drops less sharply and the slope appears to be constant. This indicates that the concentration is constant in this central riser region and denser at the far riser wall. For this example, the riser is dilute and visually clear enough for a bright light to be used to look into the unit. Over the radial span 5.08 to 7.5 cm, which is adjacent to the near riser wall, the intensity dropped very rapidly indicating that the solids concentration is very dense across this zone. It was noticed, however, that a "stagnant cluster of particles" adhered to the tip of the probe when it was used in this region, invalidating the local result. Particle clusters were not observed to adhere to the probe when it was positioned in the other regions of the riser. Because the particles appeared to cling to the probe, and/or a tranquil flow zone was created on the near side of the riser, the problem seems to be electrostatic in nature. Such a zone may be generated by the intrusive nature of the measuring technique. For dilute operating conditions, asymmetry between the near and far sides of the riser is typical of the slope of the natural logarithm of intensity vs. radial distance plots. However, the slope measured in the larger central core region of the riser is constant and symmetric with respect to both sides of the CFB. For dense operating conditions, the slope of the radial intensity profiles were practically symmetric across the entire riser radius, as shown in Figure 4. This observation is consistent with the assumption that the solid volume fraction profiles are symmetric and that electrostatics are responsible for asymmetry in the intensity data. Due to the obvious error

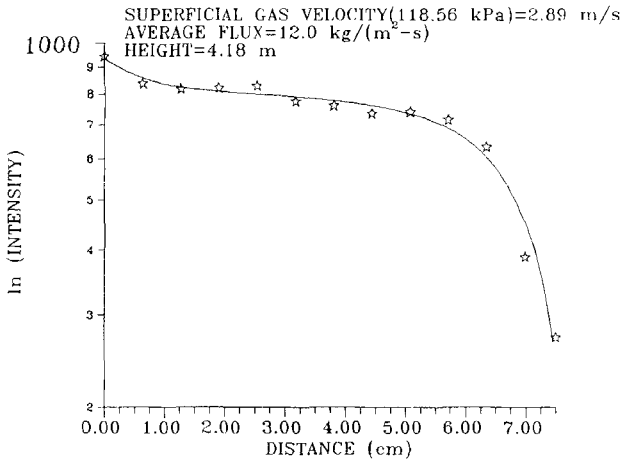

Figure 3. Typical X-ray intensity plot for dilute flow.

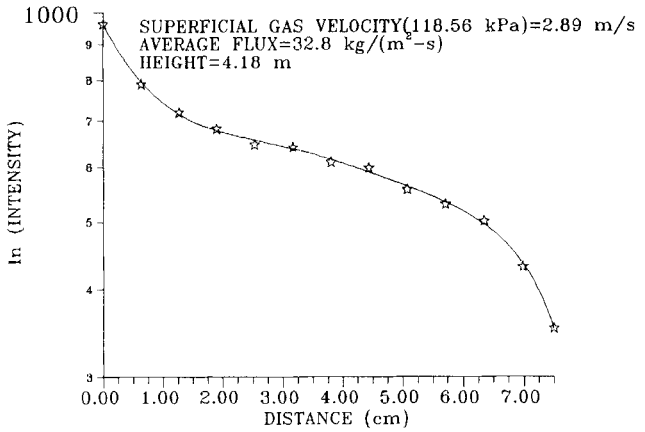

Figure 4. Typical X-ray intensity plot for dense flow.

in measurement on the near side of the riser, symmetry with the riser far side was assumed when graphing the solid volume fraction.

Extraction Probe

Apparatus

Flux profiles in the CFB were monitored with the extraction probe shown in Figure 5. The probe consists of a brass tube that has an outside diameter of 0.635 cm and a 0.4724 cm inside diameter. The tube is bent at a 90-degree angle to align its opening parallel to the flowing gas-solids mixture. Unfortunately, due to its 90-degree bend, the probe could not be pulled back flush with the near riser wall. Therefore, flux measurements spanned only 6.985 cm of the 7.5 cm riser inside diameter.

After extraction by the probe, the solids/gas mixture is separated by a filter. The filter is equipped with a removable solids collection chamber that is fabricated of clear PVC for visual observation. Air leaving the filter flows through a finer secondary filter to protect the downstream rotameter and vacuum pump. The flow rate of air exiting the extraction probe is regulated by a globe valve that is located downstream of the rotameter. Additional extraction probe fabrication details are described by Miller (1991).

Theory of operation

At any particular position within the CFB, the time-averaged flux consists of an upward and downward component. The magnitude of the upward flux minus the magnitude of the downward flux is equal to the net upward flux. The upward and downward flux are measured with the inlet of the extraction probe (Figure 5) pointing in the upstream and downstream directions, respectively. Because the CFB operates in an oscillatory state, all flux measurements were time-averaged over periods that ranged from 1.5 to 6 minutes. Flux components were calculated by dividing the weight of solids recovered in the filtration collection chamber by the area of the tip of the probe and sample time.

Van Breugel et al. (1969) suggested in their study that the extraction probe should be operated under isokinetic conditions. That is, the velocity in the probe nozzle should be equal to that of the surrounding stream to avoid disturbing the local riser flow pattern. However, circulating fluidized beds operate with large and rapid velocity fluctuations making it very difficult, if not impossible, to operate the probe isokinetically. Similar to Gajdos and Bierl (1978), we have found that the flux withdrawn by the extraction probe does not vary significantly when the probe gas extraction velocity is altered within the range of gas velocities anticipated at the local positions in the CFB. This is probably due to the overwhelming size of the momentum of the solids in comparison to that of the gas. From the analysis of the data taken in this investigation, it is deduced that the local average CFB gas velocity in Figure 6 should be roughly 1 m/s in the downward direction, assuming that the solids have reached their terminal velocity. However,

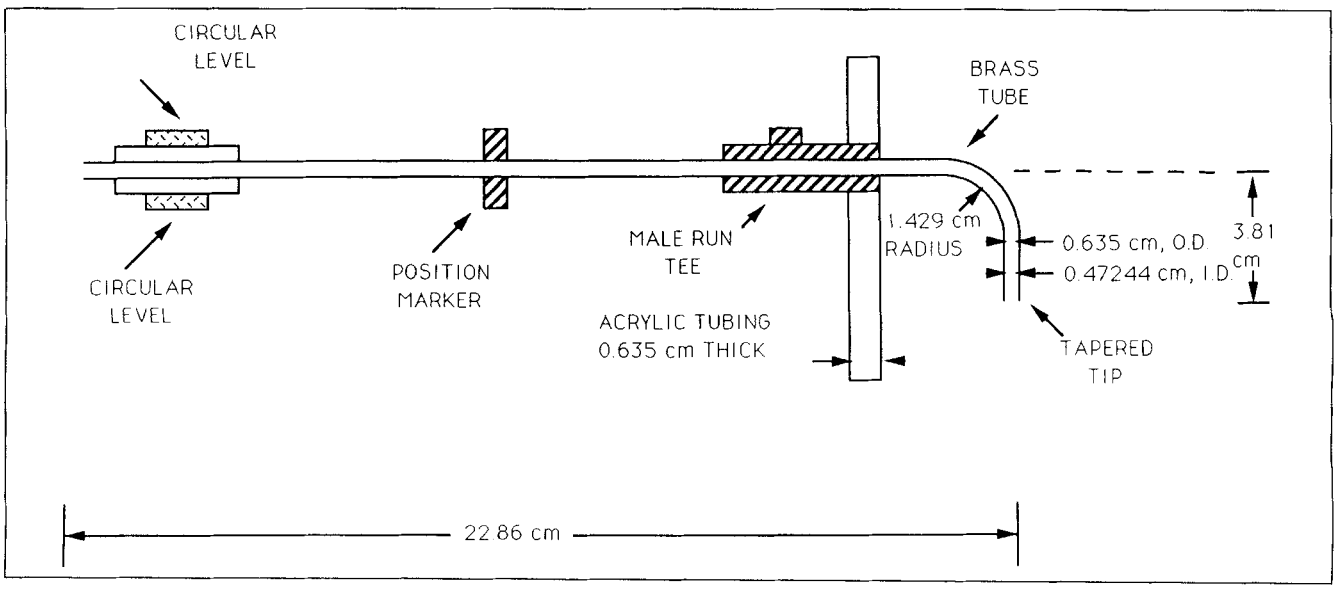

Figure 5. Extraction probe schematic.

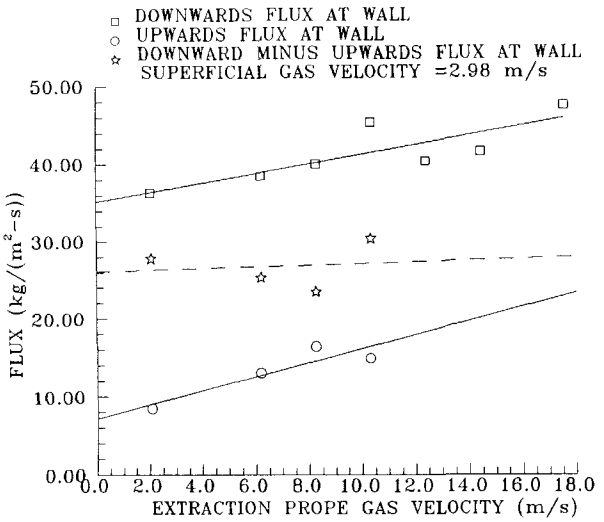

Figure 6. Typical data for flux determination at the wall.

the net downward flux varies by less than 6% between the gas extraction velocities of 0 to 4 m/s. A similar insensitivity is observed for the upward flux at the wall. There it is assumed that the time-averaged velocity should be roughly equal to zero, since the net flux is moving downward.

The magnitude of both flux components appears to be a linear function of the flow of gas through the extraction probe. However, the net flux does not. This behavior is shown in Figure 6 where a least-squares fit of the data shows the downward minus upward flux at the riser wall to be constant. Downward fluxes at the center of the riser have been negligible in comparison to their corresponding upward flux for all measured conditions of flow. In agreement with the aforementioned hypothesis, the upward flux at the riser center is insensitive to the gas flow rate.

Near the CFB wall it is necessary to measure both the downward and upward flux to obtain the net flux. Flow-restrictive plugging, however, would sometimes occur in the extraction probe when it was operated within the range of low gas velocities present at this location. There is little difference in the magnitude of the upward and downward gas velocities that are measured in the vicinity of the riser wall. The upward and downward flux components are practically equal for these changes in velocity. Therefore, in this investigation the net flux has been taken to be the difference between the two components of the flux, measured at the same gas extraction rate. To compensate for experimental error, the readings were averaged over two gas extraction rates. An attempt was made to obtain all measurements at minimal gas flow that was high enough to prevent the probe from plugging. Since "net flux" appears to be insensitive to gas extraction velocity, isokinetic sampling was not attempted for this work.

Experimental Data

Solids flux profiles

Solids flux profiles were obtained at heights of 1.86, 4.18 and 5.52 m above the riser inlet for five distinct flow conditions. The profiles are quasi-parabolic with an upward-moving mass flux at the center of the column and downward at the wall. In Figure 7, the radial mass flux is plotted at a constant superficial gas velocity of 2.89 m/s for feed fluxes of 32.8, 20.4 and 12.0 kg/m^2·s at a riser height of 4.18 m. The radial flux at the center of the pipe increases with increasing feed flux. Centerline radial fluxes of approximately 110, 80 and 37 kg/m^2·s are obtained for the respective increasing values of the feed flux. At the wall, solids are flowing downward and the magnitude of the flux increases rapidly with increasing values of the feed flux. The core is defined as the region at the center of the riser in which the net solids flux is moving upward. Figure 7 shows that intercepting zero flux values with radial distance, the radius of the core decreases with increasing values of feed flux.

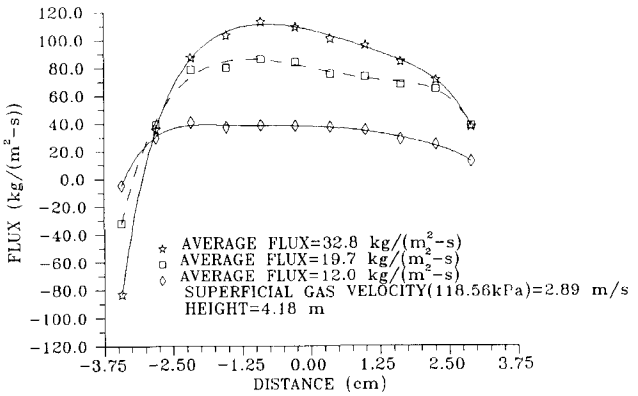

Figure 7. Radial flux profiles for various solids feed rates.

Three mass flux profiles were obtained for a constant feed flux of 20.4 kg/m^2·s at the riser height of 5.52 m. The results of the testing are shown in Figure 8 for the superficial gas velocities of 2.61, 2.89 and 3.48 m/s. The core radius increases with increasing superficial gas velocity. In the riser center, the flux decreases as the superficial gas velocity increases. The flow profiles are nearly flat for the superficial gas velocities of 2.89 and 3.48 m/s, and become parabolic when the gas velocity is lowered to 2.61 m/s. This is probably due to a higher shear viscosity that is realized in the denser system at 2.61 m/s. Also, the solids flux at the wall flows downward in increasing magnitude as the superficial gas velocity decreases resulting in higher shear rates at lower gas velocities.

Figure 9 shows radial flux profiles as a function of riser

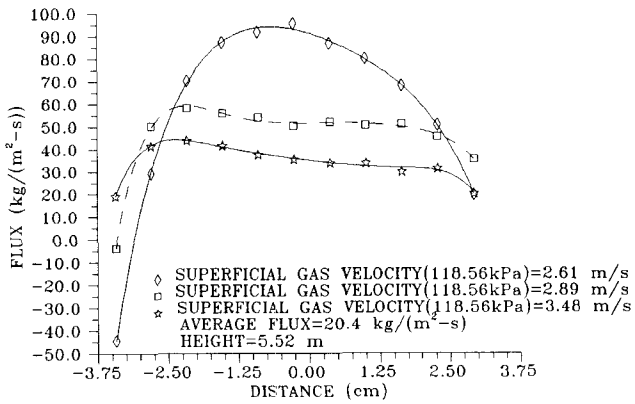

Figure 8. Radial flux profiles for various gas flow rates.

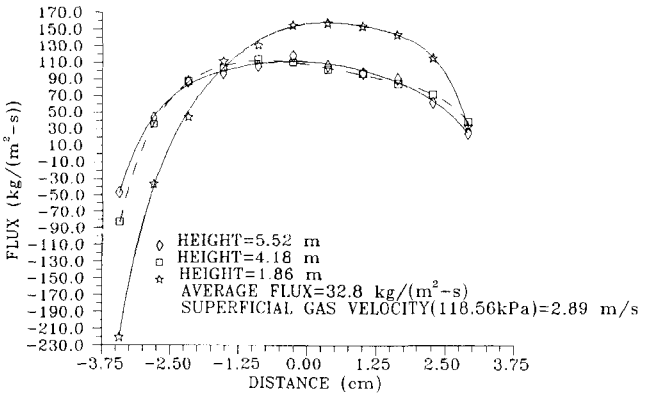

Figure 9. Radial flux profiles for various riser heights.

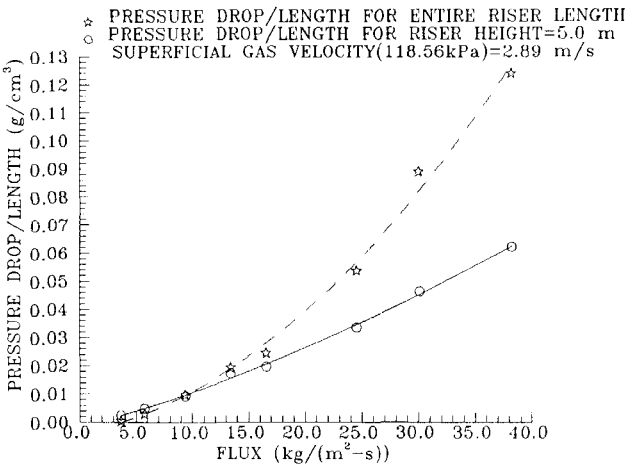

Figure 11. Apparent density ($\Delta P/L$) as a function of solids feed rate.

height when the superficial gas velocity equals 2.89 m/s and the riser feed flux equals 32.8 kg/m^2·s. The magnitude of fluxes measured in both the upflowing core and downflowing annulus decreases with increasing riser height. In this plot, as well as in plots taken under other operating conditions (see Miller, 1991), the core radius always increases with riser height.

Solids Volume Fraction Profiles

Solid volume fraction and flux profiles were acquired for each condition of operation. In Figure 10, radial solid volume fraction is plotted at a constant superficial gas velocity of 2.89 m/s for the feed fluxes of 32.8, 20.4 and 12.0 kg/m^2·s at the riser height of 5.52 m. The volume fraction is constant in the center of the riser and rises at the wall. The solids volume fraction across the entire riser diameter increases with increasing values of the feed flux. This is consistent with $\Delta P/L$ measurements (Figure 11) which increase with increases in feed flux. In Figure 12, radial solid volume fraction is plotted at a constant feed flux of 20.4 kg/m^2·s for the superficial gas velocities of 2.61, 2.89 and 3.48 m/s at a riser height of 1.86 m. The solid volume fraction increases across the entire riser diameter when the superficial gas velocity is decreased. There is a sharp increase in the solid volume fraction when the superficial gas velocity is lowered to 2.61 m/s. As shown in Figure 13, these trends are consistent with riser $\Delta P/L$ measurements that increase as the superficial gas velocity decreases and increase sharply at the gas velocity of 2.61 m/s.

In Figure 14 radial solid volume profiles are plotted as a function of riser height when the CFB is operated at a superficial gas velocity of 2.61 m/s and average solids feed flux of 20.4 kg/m^2·s. At the lower riser height of 1.86 m, the riser is densely packed and the flow is nearly bubbling. The average solid volume fraction at this height is 0.091. As we move up the column to 4.18 m, there is a transition from what visually appears to be bubbling to co-annular flow. That is, visual observation shows that the net flow of particles at the riser wall is rapidly falling downward. The average solid volume fraction at this height is 0.032 which is significantly lower than that measured at 1.86 m. Contrary to the established trend, the average solids volume fraction at 5.52 m is greater than that measured at 4.18 m, but less than that measured at 1.86

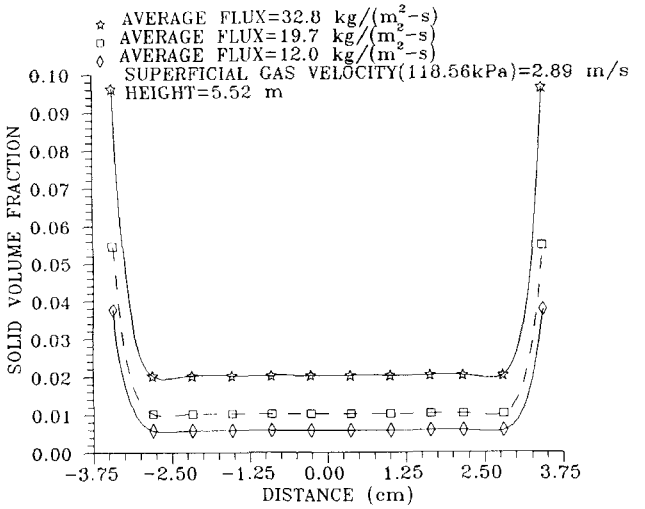

Figure 10. Radial solids concentration profiles for various solids feed rates.

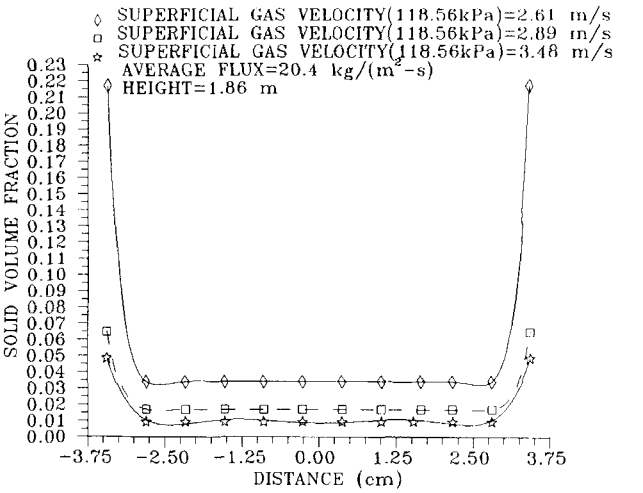

Figure 12. Radial solids concentration profiles for various gas flow rates.

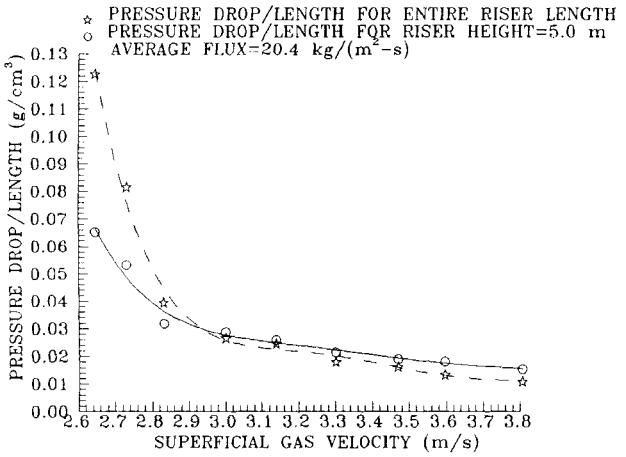

Figure 13. Apparent density ($\Delta P/L$) as a function of gas flow rate.

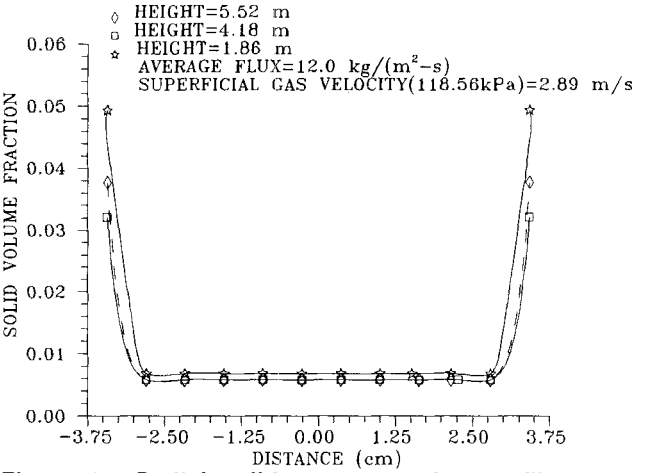

Figure 15. Radial solids concentration profiles as a function of riser height for dilute operation of the riser.

m. This pattern is typical of the data obtained (Miller, 1991) and repeated in Figure 15 when the CFB is operated dilute at a superficial gas velocity of 2.89 m/s and solids feed flux of 12.0 kg/m^2·s. Pressure drop/length ($\Delta P/L$) measurements along the length of the riser support these trends as shown in Figure 16. Similar trends were also observed by Wu et al. (1989) who contributed them to exit effects. Werther et al. (1990) used optical methods to determine radial particle concentration in a CFB. Their data also show dense regions near the riser wall and particle concentrations that decrease with riser height. Pressure drop measurements were 3 ft (0.9 m) or less, and the measurements at the two upper heights were obtained simultaneously with a computerized data acquisition system. From these measurements, as well as the solids flux profiles, it appears that fully developed flow does not occur in the riser in spite of its large length/diameter (L/D) ratio of 84.

Solids Velocity Profiles

Solids velocity profiles are obtained indirectly from the solids flux and solids volume fraction profiles by the algebraic relationship:

$$V_s = F_s/(\rho_s \epsilon_s) \tag{2}$$

That is, the solids velocity at any radial position is equal to the solids flux divided by the particle density and solid volume fraction. In Figure 17, radial solids velocity profiles are plotted at a constant superficial gas velocity of 2.89 m/s for the solid feed fluxes of 12.0, 20.4 and 32.8 kg/m^2·s, at the riser height of 1.86 m. Velocities measured in the upflowing core are between 2 and 4 m/s and increase with decreases in feed flux. The velocity of solids in the downflowing annulus varies between -0.5 and -1.5 m/s and increases in magnitude with decreasing feed flux. In agreement with solids flux profiles obtained at this height (Miller, 1991), the core radius is nearly the same for each feed flux. This observation changes as we proceed up the riser to a height of 4.18 m (Figure 18). At this height the magnitude of velocities measured in the core and annulus increases with increases in feed flux, while the core

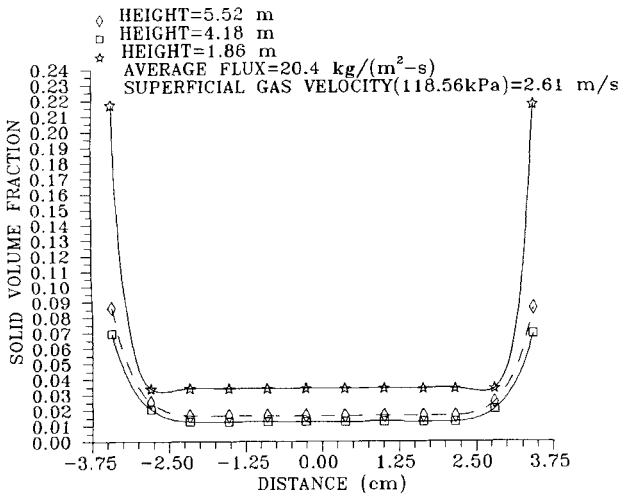

Figure 14. Radial solids concentration profiles as a function of riser height for dense operation of the riser.

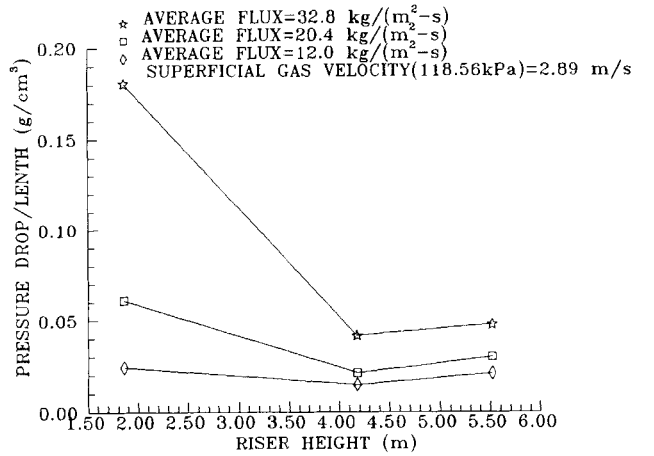

Figure 16. Apparent density ($\Delta P/L$) vs. riser height as a function of solids feed rate.

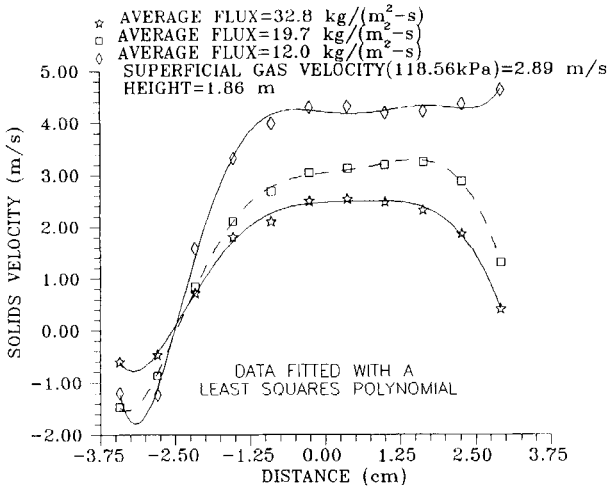

Figure 17. Radial solids velocity for various solids feed rates at the lower riser height.

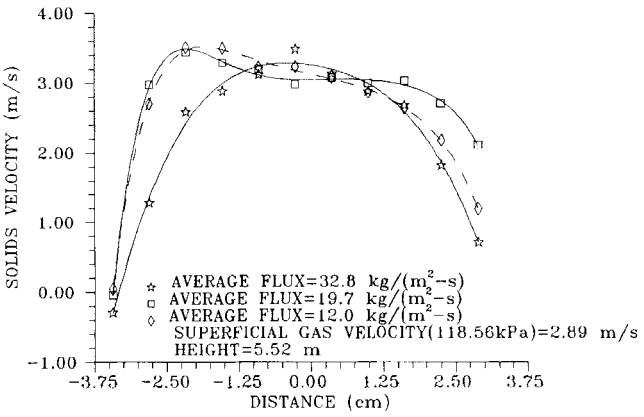

Figure 19. Radial solids velocity for various solids feed rates at the upper riser height.

radius decreases. For the riser height of 5.52 m (Figure 19), the solids velocity deviates only slightly from 3 m/s for all three feed conditions in the center of the riser. The magnitude of solids velocities in the riser annulus increases with augments in feed flux and deviates between 0 and -0.35 m/s. Deviations in the riser core are less significant with velocity tending to increase with decreases in feed flux.

Solids velocity profiles are plotted in Figures 20, 21 and 22 at the respective heights of 1.86, 4.18 and 5.52 m for the solids feed flux of 20.4 kg/m^2·s and superficial gas velocities of 2.61, 2.89 and 3.48 m/s. At the height of 1.86 m solids velocities differ slightly in the core and annulus with lower solids velocity measured at correspondingly lower superficial gas velocities. When the height is increased to 4.18 m, the aforementioned trend continues for the superficial gas velocities of 2.61 and 2.89 m/s, which have core velocities of approximately 4.0 and 5 m/s, respectively. When the gas velocity is increased to 3.48 m/s instead of continuing in this trend the core velocity reduces to 3.5 m/s. This may be due to the large expansion of the core that takes place at this velocity. Because the annulus is significantly smaller, "less material" is recycled up the "larger core" allowing the net upward mass to flow at a lower solids velocity. For the height of 5.52 m, radial solids velocities differ significantly and are correspondingly lower at lower superficial gas velocities across the entire profile. The radius of the core increases with increasing gas velocity at all riser heights.

Radial solids velocity as a function of riser height is shown in Figure 23 when the superficial gas velocity equals 2.89 m/s and solids feed flux equals 32.8 kg/m^2·s. Solids velocities are lowest at the lower height of 1.86 m in both the annulus and core. In spite of an expansion of the core, solid velocities significantly accelerate across the entire riser profile as we proceed up the riser height to 4.18 m. At the riser height of 5.52 m, the magnitude of the solids velocity significantly decreases in the downward flowing annulus and upward flowing core, resulting in a much flatter profile. This is typical of most of the experimental data and is shown to occur also in Figure 24 for the superficial gas velocity of 2.89 m/s when the feed flux equals 20.4 kg/m^2·s. An exception to this pattern occurred when the superficial gas velocity was increased to 3.48 m/s. As shown in Figure 25, solids velocities increased over the entire flow diameter with increases in riser height. The core radius increased with increases in riser height for all observed flow conditions.

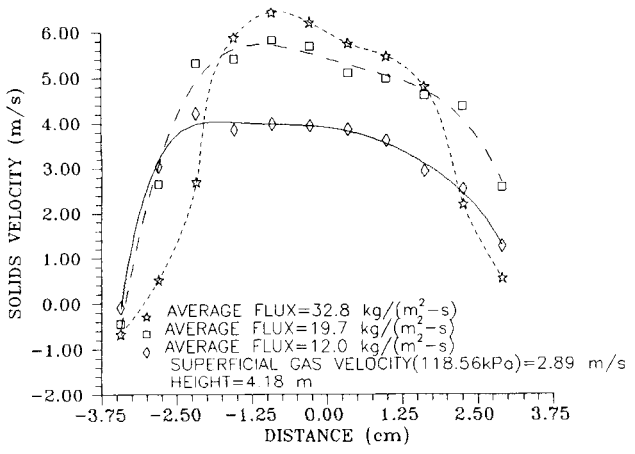

Figure 18. Radial solids velocity for various solids feed rates at the middle riser height.

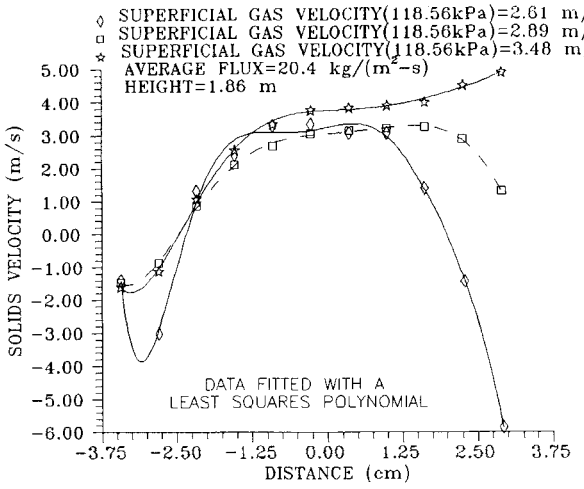

Figure 20. Radial solids velocity for various gas feed rates at the lower riser height.

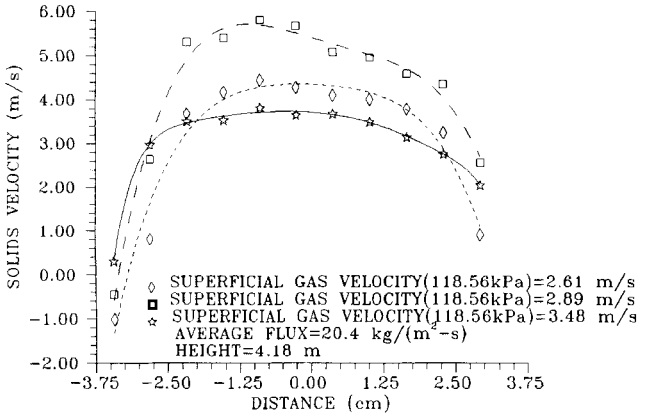

Figure 21. Radial solids velocity for various gas feed rates at the middle riser height.

Solids Viscosity

The mixture momentum balance for the CFB may be written as (Tsuo and Gidaspow, 1990):

$$\frac{\partial(\epsilon_s \rho_s V_s^2 + \epsilon_g \rho_g V_g^2)}{\partial z} = -\frac{\partial P}{\partial z} + \frac{1}{r}\frac{\partial}{\partial r}\left(r\left(\mu_s \frac{\partial V_s}{\partial r} + \mu_g \frac{\partial V_g}{\partial r}\right)\right) - (\epsilon_s \rho_s + \epsilon_g \rho_g)g \quad (3)$$

Based on the experimentally verified assumptions that the density of the solid phase is much greater than that of the gas phase, the viscosity of the solids phase is much greater than that of the gas phase, and the hypothesis that the radial solids velocity and velocity gradient are of the same order of magnitude as the radial gas velocity and velocity gradient, the following equation is obtained:

$$\frac{\partial(\epsilon_s \rho_s V_s^2)}{\partial z} = -\frac{\partial P}{\partial z} + \frac{1}{r}\frac{\partial}{\partial r}\left(r\mu_s \frac{\partial V_s}{\partial r}\right) - \epsilon_s \rho_s g \quad (4)$$

This momentum balance is illustrated in Figure 26. Measurements indicate that the pressure (P) is a negligible function

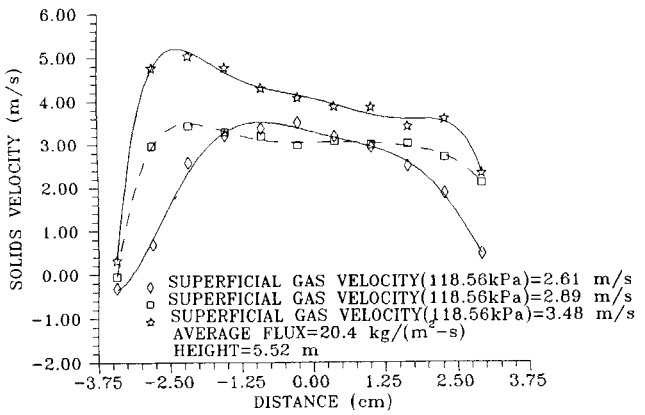

Figure 22. Radial solids velocity for various gas feed rates at the upper riser height.

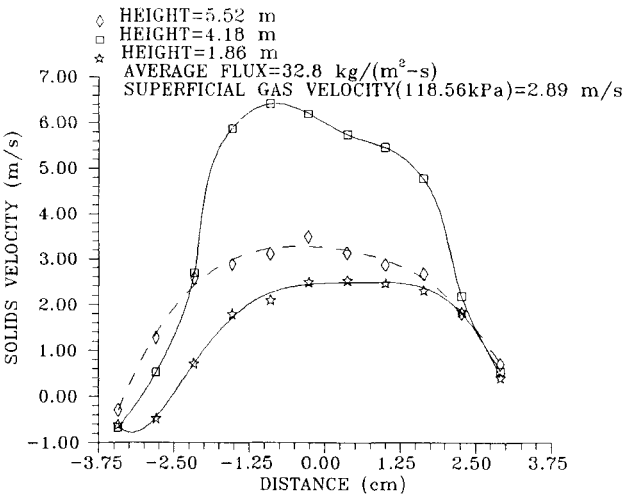

Figure 23. Radial solids velocity for various riser heights at a superficial gas velocity of 2.89 m/s and solids feed rate of 32.8 kg/m²·s.

of the radial position. Also assuming that the solids velocity gradients are symmetric across the riser, the following equation is obtained after integration and algebraic manipulation:

$$\frac{2}{R^2}\int_0^R \frac{\partial(\epsilon_s \rho_s V_s^2)}{\partial z} r dr - \frac{2}{R}\mu_s \frac{\partial V_s}{\partial r}\bigg|_{r=R} = -\frac{\partial P}{\partial z} - \frac{2}{R^2}\int_0^R \epsilon_s \rho_s r dr \quad (5)$$

This equation states that the pressure drop minus the weight of the bed is equal to the shear plus the axial acceleration for any position R. The shear rate is evaluated as the derivative of the velocity profile with respect to radial position. An algebraic formula for the velocity is obtained by approximating the data with the least-squares polynomial that visually best fits the profile. The polynomial ranged in order from the 5th to 8th degree. The axial acceleration and weight of the bed were also determined directly from integration of the solid volume fraction, velocity and flux profiles for any particular radial

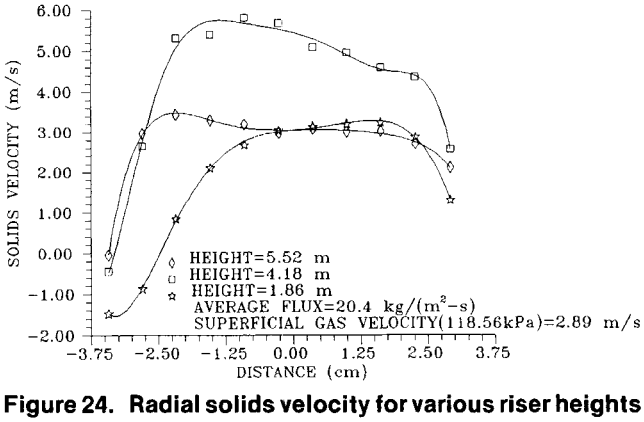

Figure 24. Radial solids velocity for various riser heights at a superficial gas velocity of 2.89 m/s and solids feed rate of 20.4 kg/m²·s.

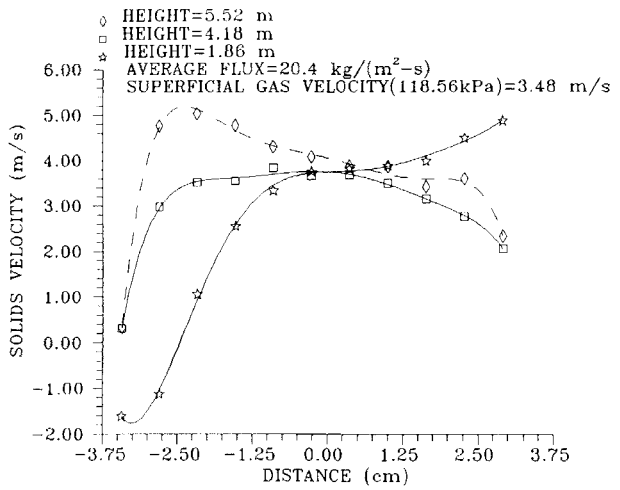

Figure 25. Radial solids velocity for various riser heights at a superficial gas velocity of 3.48 m/s and solids feed rate of 20.4 kg/m²·s.

position. Axial pressure gradients were obtained with a computerized data acquisition system over a length that varied from 69.85 to 91.44 cm. To determine the solids viscosity, Eq. 5 was evaluated across the riser radius in increments of 0.0635 cm for each of 15 distinct velocity profiles, that were obtained at different heights, feed fluxes, and superficial gas velocities. For each flow profile there was a region in which the viscosity did not vary much with changes in radial position. This always

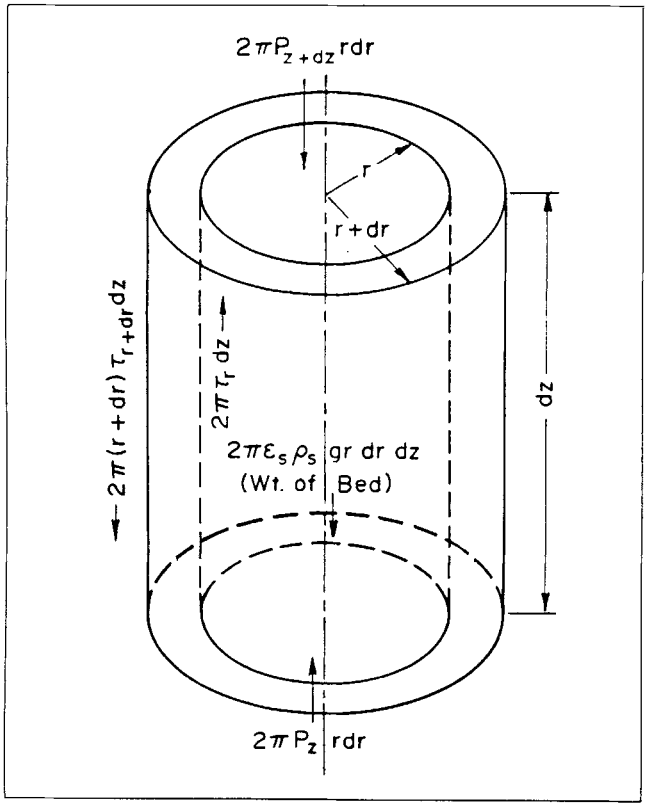

Figure 26. Momentum balance for viscosity determination.

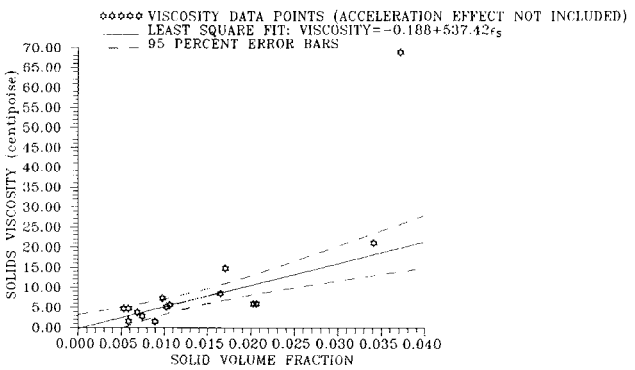

Figure 27. Particle viscosity correlation without acceleration effects with 95% confidence levels.

occurred in the transition region between the core and annulus, where the shear rate was high and well defined due to the large change in velocity between data points. The average viscosity and solid volume fraction across this region has been taken as being unbiased and correlatable. In Figure 27 the solids viscosity is plotted vs. solid volume fraction for each flow profile when acceleration effects are not taken into account. Figure 28 is a similar plot, but with acceleration included in the correlation. Though a least-squares fit of the data is essentially the same for both cases, the error bars and data are significantly closer to the regression line when acceleration is taken into account, demonstrating the need to include this term. Similar to Tsuo and Gidaspow (1990), the viscosity can be approximated by the solid volume fraction multiplied by a coefficient of 5.35 poise. The measured viscosity for the solid volume fraction of 0.038 is significantly above the regression line, and therefore is not included in the correlation. This undesirable circumstance is lessened when we attempt to take acceleration into account. There was a sharp transition in concentration from what in appearance was bubbling to co-annular fluidization at a location that was less than 0.5 m above the aforementioned data acquisition point. However, the approximation for acceleration spanned 2.32 m. Therefore, the acceleration used in the calculation may have been severely underestimated and may account for the large deviation of the data point from the regression line. A detailed calculation of the solids viscosity is shown in the Appendix.

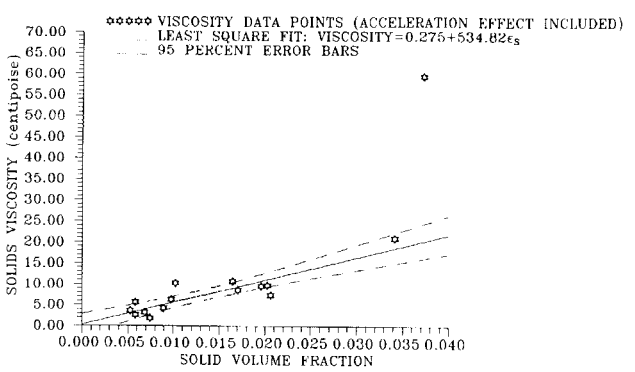

Figure 28. Corrected particle viscosity correlation with 95% confidence levels.

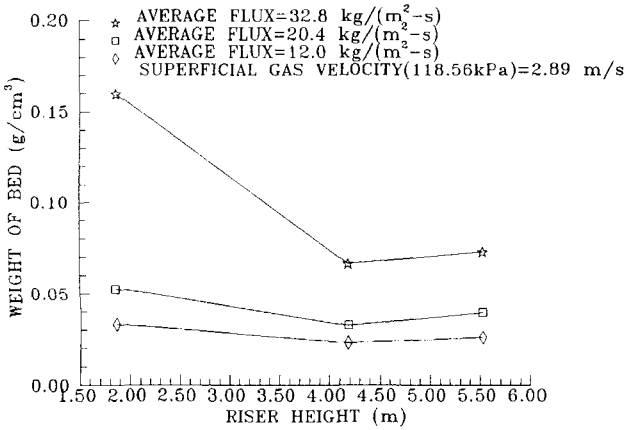

Figure 29. X-ray determined axial bed weight vs. riser height for various solids feed rates.

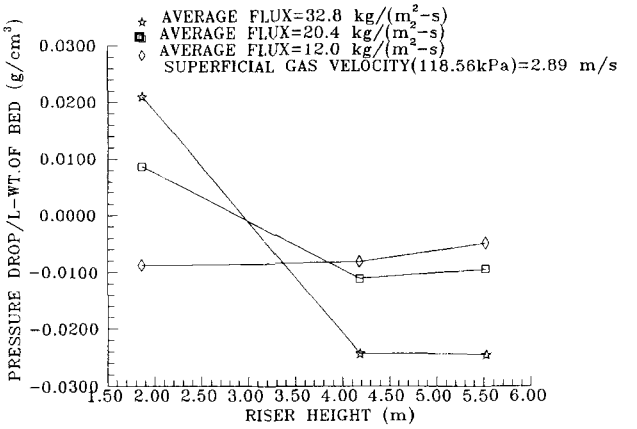

Figure 30. Apparent density ($\Delta P/L$) minus X-ray determined axial bed weight vs. riser height for various solids feed rates.

Discussion of Flow Profiles

An apparent density ($\Delta P/L$) measurement was obtained for each solid volume fraction profile. Assuming that the pressure drop is equal to the weight of the bed, several investigators have used this value as the mean riser density over the axial location of measurement. Riser pressure drops for apparent density measurements were obtained with a computerized data acquisition system that was central to the solid volume fraction measurement over a length that varied from 69.85 to 91.44 cm and at a sampling rate of 6 to 25 Hz. In Figure 16, apparent density is plotted vs. riser height for several feed fluxes at the superficial gas velocity of 2.89 m/s. As anticipated from the solid volume fraction profiles, the apparent density is highest at the riser inlet and lowest for the central measurement location. Also the density decreases and becomes less of a function of riser height with decreases in solids feed flux. The weight of the bed (actual density) for axial locations was obtained by multiplying the density of the catalyst particles by the integral mean of the solid volume fraction profiles as follows:

$$\frac{2}{R_w^2}\int_0^{R_w} \epsilon_s \rho_s \, r dr \tag{6}$$

The data are plotted in Figure 29 and compare favorably in magnitude and shape with the apparent density profiles. The deviation of the apparent density ($\Delta P/L$) from the weight of the bed is shown in Figure 30 vs. riser height. The deviation is positive at the lower riser height, with the exception of the profile for the low flux condition. At the upper riser heights the deviation is always negative. If we assume that the pressure drop minus the weight of the bed is equal to the shear at the wall, the negative deviations are consistent with negative wall shears that have been reported (Van Swaaij et al., 1970) and the downflow along the riser wall that "must produce a negative shear" for conformity with a no-slip or partial-slip wall boundary condition. Positive deviation of the pressure drop from the weight of the bed suggests that in addition to the shear the system is accelerating. This effect is clearly shown by the velocity profiles in Figures 23 and 24 that correspond to the positive deviations. From inspection it is evident that the fluid is accelerated in moving from the lower to the middle height. Assuming that the shear at the wall can be represented as follows:

$$-\mu \left.\frac{\partial V_s}{\partial r}\right|_{r=R_w} = \frac{R_w}{2}\left(-\frac{\partial P}{\partial z} - \frac{2}{R_w^2}\int_0^{R_w} \epsilon_s \rho_s \, r dr - \frac{2}{R_w^2}\int_0^{R_w} \frac{\partial(\epsilon_s \rho_s V_s^2)}{\partial z} r dr\right) \tag{7}$$

These trends appear to be constant with the measured relationship among pressure drop, viscosity, density and velocity. Wall shear stress is plotted in Figure 31 for the superficial gas velocity of 2.89 m/s when the feed fluxes equal 12.0, 20.4 and 32.8 kg/m^2·s. The shear stress is increasingly negative in the two upper riser sections, where acceleration is less important, for larger values of feed fluxes. From inspection of the velocity profiles, the annulus falls at increasingly higher velocities for the riser upper and middle sections as the feed flux increases. Assuming a no-slip or partial-slip boundary condition, this suggests that the magnitude of the wall shear rate increases also. The solids viscosity increases with increasing feed flux,

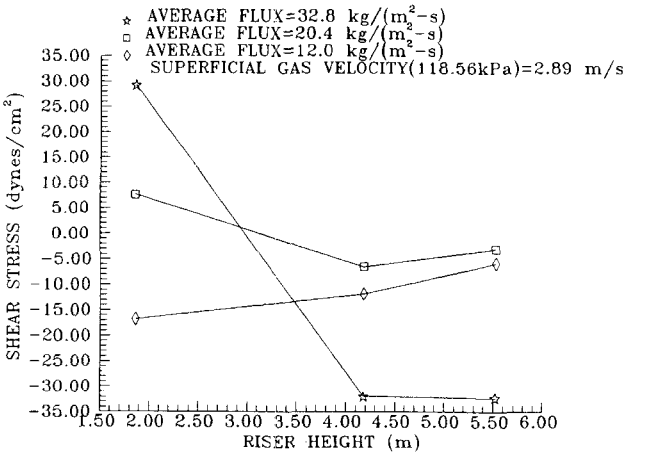

Figure 31. Computed shear stress as a function of riser height for various solids feed rates.

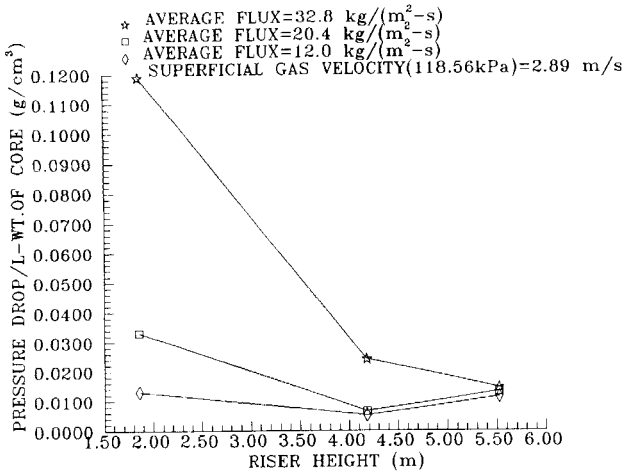

Figure 32. Apparent density ($\Delta P/L$) minus X-ray determined weight of riser core vs. riser height for various solids feed rates.

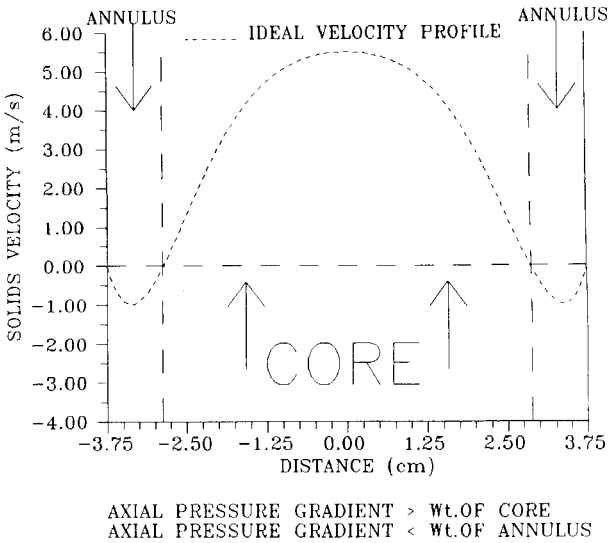

Figure 33. Schematic of an idealized particle velocity profile in the riser.

since the solid volume fraction grows larger. Since the wall shear stress is a product of the shear rate and viscosity the trend shown for the two upper riser sections in Figure 31 is expected.

Though the pressure drop minus the weight of the bed can be negative, the pressure drop minus the weight of the upflowing core was always found to be positive, as it must be to achieve an upward motion. These data are plotted in Figure 32. Note that at the bottom of the bed the deviation is much greater than at the middle and upper sections, which is consistent with large acceleration effects in the lower bed section. In the annulus the pressure drop was always less than the weight of the bed which is in agreement with the net downward flow of particles there. An illustrative velocity profile is shown in Figure 33 that assumes a no-slip boundary condition at the wall. The figure can be summarized as follows:

1. The pressure drop is always greater than the weight of the core.

2. The pressure drop is always less than the weight of the annulus.

3. The shear at the wall is always negative when there exists a downflowing annulus, as it must be for consistency with a no-slip or partial-slip wall boundary condition.

Visual inspection of the riser flux and velocity profiles shows that the radius of the core always increased with increased riser height. A significant increase occurs between the lower and middle heights, especially when the riser is operated under dense flow conditions. Typical core radius values are 2.5, 3.05 and 3.35 cm for the respective heights of 1.86, 4.18 and 5.52 m as interpolated from Figure 23 for dense operation of the riser. For the less dense operation in Figure 24, typical core radius values are 2.5, 3.35 and 3.40 cm for the same respective heights. The following characteristics of the core radius were observed:

1. The radius of the core always decreases when the feed flux was increased.

2. The radius of the core always decreased when the superficial gas velocity was decreased.

3. The radius of the core always increased with increased riser height.

For gas velocities less than 0.4 m/s, the slip velocity for the average 75-μm particles used in this analysis is 0.275 m/s. Since this value is low as compared to the measured solids velocities, it may be possible to infer the location of the gas core from knowledge of the measured (solids) core. In this investigation, the gas core is assumed to be the radius obtained from the intersection of the negative of the slip velocity with the velocity curves. As previously stated, the radius of the core increases with increased riser height and the total mass flow rate of solids in the annulus decreases. To satisfy the continuity equation, the total mass flow rate of solids in the core must decrease with riser height. In Figure 23, gas core radius values of 2.75, 3.25 and 3.75 cm for the respective heights of 1.86, 4.18 and 5.52 m are interpolated for dense operation of the riser. It is evident, as previously stated, that at the height of 1.86 m, the solids are being accelerated since the measured solids velocity is well below the superficial gas velocity at all points on the curve. At the height of 4.18 m, measured solids velocities increased and were as large as 6 m/s in the parabolic shaped core. This value is reasonable when we take into account that all of the upward flowing gas flows in the gas core which is only 75% of the riser pipe area and that the volumetric total of the upward flowing gas is the sum of the gas input into the riser plus the amount recycled down the annulus. At the height of 5.52 m, the measured gas velocities decreased significantly in the core. Solids velocities measured in the center of the core were slightly larger than the superficial gas velocity. This behavior appears to be consistent when it is taken into account that the gas core traverses virtually all of the riser diameter. Assuming a parabolic shape for the gas velocity profile, it is not unreasonable to assume that a mass balance would show that the gas velocity profile could be reasonably constructed by adding the slip velocity to the solids velocity.

In general, measured solids velocities are within the range of velocities that would be anticipated by assuming the gas velocity is equal to the solids velocity plus slip velocity. At upper riser heights it appears that the gas annulus significantly shrinks to a small or insignificant size, and therefore the gas

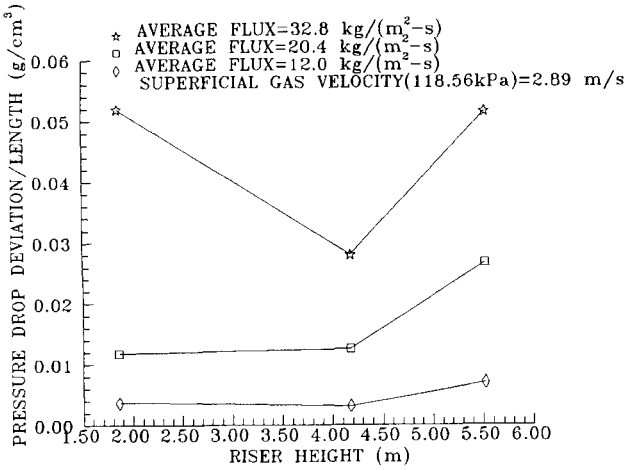

Figure 34. Standard deviation of the pressure drop per unit length as a function of riser height.

velocity must also decrease, possibly significantly. Though the solids velocity is limited by its neighboring gas velocity, the density of solids is not. Since the solids velocity decreases at the upper riser height from the continuity equation, the density of solids must increase to maintain the same net solids outflow as measured at other riser axial locations. This may be the reason that apparent density and weight of the bed profiles both show the bed density which is greater at the riser outlet than for its middle section. These phenomena were also observed by Wu et al. (1989) who contributed them to exit effects.

The mean deviation of the apparent density is plotted in Figure 34 for the constant superficial gas velocity of 2.89 m/s. The deviations increase with feed flux and riser height with the exception of the high feed flux profile which has a high apparent density deviation at the riser inlet. However, when the apparent density deviation divided by the mean apparent density is plotted vs. riser height for the same operating conditions, a straight line plot is achieved for all feed flux conditions as shown in Figure 35. This drawing clearly shows that the oscillations increase with feed flux and riser height. At the

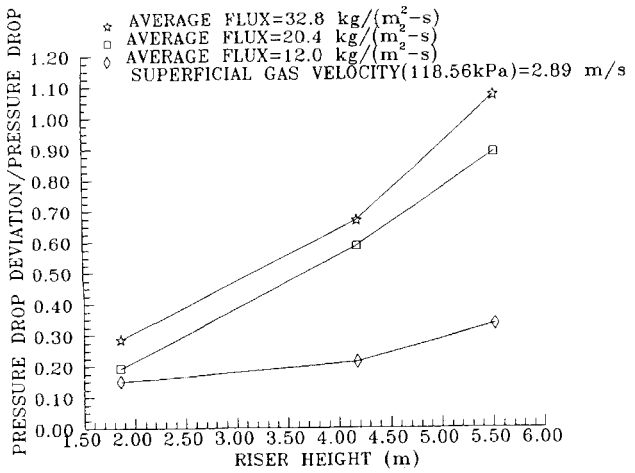

Figure 35. Relative deviation of the pressure drop per unit length as a function of riser height.

riser outlet for the feed flux of 32.8 kg/m²·s, the mean deviation is even greater than its mean. The pressure fluctuations increase with riser height, as does the radius of the core and along with a reduction in the mass flow rate may be the mechanism for core expansion. At the lower riser height the pressure oscillations are smaller, possibly due to the dampening effect of the solids in the upper portion of the riser. As the riser height increases, the ability of the riser to dampen the oscillations becomes less and therefore we observe the behavior shown in Figure 35.

Acknowledgment

The authors would like to thank the sponsors of the Illinois Minority Graduate Incentive Program for providing a fellowship to complete this work. Partial support was also provided by the Department of Energy University Coal Research, grant no. DE-FG-22-89PC89769 and Institute of Gas Technology, subcontract no. S1-17150.

Notation

F_s = flux of solids
g = acceleration due to gravity
h = riser height location
I = incident colinear x-ray beam of intensity I counts/s
L = axial length for evaluation of pressure drop
P = gas pressure
R = radial position of equation evaluation
R_w = pipe inner wall radius
r = radial cylindrical coordinate
t = thickness of gas/solids absorber
V_g = gas velocity
V_s = solids velocity
z = axial cylindrical coordinate

Greek letters

υ_a = mass-absorption coefficient of air
υ_s = mass-absorption coefficient of solids
ϵ_g = gas volume fraction
ϵ_s = solids volume fraction
ρ_a = air density
ρ_g = gas density
ρ_s = density of solid particles
μ_g = viscosity of gas phase
μ_s = viscosity of solid phase

Literature Cited

Bader, R., J. Findlay, and T. M. Knowlton, "Gas/Solid Flow Patterns in a 30.5-cm Diameter Circulating Fluidized Bed," *Circulating Fluidized Bed Technology: II*, P. Basu and J. F. Large, eds., Pergamon Press, p. 123 (1988).

Ding, J., and D. Gidaspow, "A Bubbling Fluidization Model Using Kinetic Theory of Granular Flow," *AIChE J.*, **36**, 523 (1990).

Engstrom, F., "Future Challenges of Circulating Fluidized Bed Combustion Technology," PL3-1, Preprints Int. Conf. on Circulating Fluidized Beds, Nagoya, Japan (Oct., 1990).

Gajdos, L. J., and T. W. Bierl, "Studies in Support of Recirculating Bed Reactors for the Processing of Coal," Annual Report, Prepared U.S. Dept. of Energy, FE-2449-8 (Sept. 8, 1978).

Galtier, P. A., R. J. Pontier, and T. E. Patereaux, "Near Full-Scale Cold Flow Model for the R2R Catalytic Cracking Process," *Fluidization VI*, p. 17, J. R. Grace, L. W. Shemilt, and M. A. Bergougnou, eds., Engineering Foundation, New York (1989).

Gidaspow, D., R. Bezbaruah, A. Miller, and U. Jayaswal, "Dense Transport and Fluidization of Solids in a Gas or Liquid Using Kinetic Theory," Joint DOE/NSF Workshop on Flow of Particulates and Fluids, Worcester, MA. (Oct., 1991).

Gidaspow, D., R. Bezburuah, and J. Ding, "Hydrodynamics of Circulating Fluidized Beds: Kinetic Theory Approach," *Fluidization*

VII, p. 75, O. E. Potter and D. J. Nicklin, eds., Engineering Foundation, New York (1992).
Grace, J. R., J. Zhao, R. Wu, R. Senior, R. Legros, C. M., H. Brereton, and C. J. Lim, "Spatial Variations Inside a Pilot Scale CFB Unit, 10-1 to 10-21," *Proc. Workshop on Materials Issues in Circulating Fluidized Bed Combustors*, Electric Power Research Institute, EPRI GS-6747 (Feb., 1990).
Kwauk, M., W. Ningdre, L. Youchu, C. Bingyu, and S. Zhigun, "Fast Fluidization at ICM," p. 33, *Circulating Fluidized Bed Technology*, P. Basu, ed., Pergamon Press, New York (1986).
Louge, M. Y., E. Mastorakos, and T. J. Jenkins, "The Role of Particle Collisions in Pneumatic Transport," *J. Fluid Mechanics*, **23**, 345 (1991).
Miller, A. L., "Dense Vertical Gas-Solid Flow In a Pipe," PhD Diss., Illinois Institute of Technology, Chicago (1991).
Potter, O. E., and D. J. Nicklin, eds., *Fluidization VII*, Engineering Foundation, New York (1992).
Rhodes, M. J., T. Hirama, G. Cerutti, and D. Geldart, "Non-Uniformities of Solids Flow in Risers of Circulating Fluidized Beds," p. 73, *Fluidization VI*, J. R. Grace, L. W. Shemilt, and M. A. Bergougnou, eds., Engineering Foundation, New York (1989).
Savage, S. B., "Granular Flows at High Shear Rates," p. 339, *Theory of Dispersed Multiphase Flow*, R. E. Meyer, ed., Academic Press, (1983).
Sinclair, J. L., and R. Jackson, "Gas-Particle Flow in a Vertical Pipe with Particle-Particle Interactions," *AIChE J.*, **35**, 1473 (1989).
Squires, A. M., M. Kwauk, and A. A. Avidan, "Fluid Beds: At Last, Challenging Two Entrenched Practices," *Sci.*, **230**, 4732, 1329 (1985).
Tsuji, Y., Y. Morikawa, and H. Shiomi, "LDV Measurements of an Air-Solid Two-Phase Flow in a Vertical Pipe," *J. Fluid Mech.*, **139**, 417 (1984).
Tsuo, Y. P., and D. Gidaspow, "Computation of Flow Patterns in Circulating Fluidized Beds," *AIChE J.*, **36**, 885 (1990).
Van Breugel, J. W., J. J. M. Stein, and R. J. DeVries, "Isokinetic Sampling in a Dense Gas-Solids Stream," *Joint Symp. on Fluid Mech. and Measurements in Two-Phase Flow Systems*, The Institution of Mechanical Engineers, Leeds (Sept., 1969).
Van Swaaij, W. P. M., C. Buurman, and J. W. Van Breugel, "Shear Stresses on the Wall of a Dense Gas-Solids Riser," *Chem. Eng. Sci.*, **25**, 1818 (1970).
Weinstein, H., M. Shao, M. Schnitzlein, and R. A. Graff, "Radial Variation in Void Fraction in a Fast Fluidized Bed," p. 329, *Fluidization V*, K. Ostergaard and A. Sorensen, eds., Engineering Foundation (1986).
Werther, J., E.-U. Hartge, and D. Rensner, "Measuring Techniques For Gas/Solid Fluidized Bed Reactors," *Chem. Ing. Tech.*, **62**, 605 (1990).
Wu, R. L., C. J. Lim, and J. R. Grace, "The Measurement of Instantaneous Local Heat Transfer Coefficients in a Circulating Fluidized Bed," *Can. J. of Chem. Eng.*, **67**, 301 (1989).
Yerushalmi, J., "High Velocity Fluidized Beds," Ch. 7, *Gas Fluidization Technology*, D. Geldart, ed., Wiley, New York (1986).

Appendix: Example Solids Viscosity Calculation

The data for this example were obtained at a riser height of 4.18 m when the superficial gas velocity equaled 3.48 m/s and the feed flux equaled 20.4 kg/m^2·s. From Eq. 5 the solids viscosity is calculated from the following expression:

$$\mu_s = \left(\frac{-R}{2\left(\frac{\partial V_s}{\partial r}\Big|_{r=R}\right)}\right)\left(-\frac{\partial P}{\partial z}-\frac{2}{R^2}\int_0^R \epsilon_s \rho_s\, rdr - \frac{2}{R^2}\int_0^R \frac{\partial(\epsilon_s \rho_s V_s^2)}{\partial z}\, rdr\right) \quad \text{(A1)}$$

The pressure drop was measured across a distance of 91.44 cm, central to the point at which the corresponding flux, velocity, and density was obtained. The time-averaged pressure difference across this length is 1.861 cm of water. Therefore, the axial pressure gradient is:

$$-\frac{\partial P}{\partial z}=\frac{1.861\text{ cm}}{91.44\text{ cm}}(1\text{ g/cm}^3)=0.02035\text{ g/cm}^3 \quad \text{(A2)}$$

The weight of the bed is:

$$\frac{2}{R^2}\int_0^R \epsilon_s \rho_s\, rdr \quad \text{(A3)}$$

All of the flow profiles were measured in incremental lengths of 0.635 cm. Due to this incremental method of obtaining data, the weight of the bed is approximated as:

$$\frac{2}{R_N^2}\left\{\frac{\epsilon_{s1}\rho_s R_1^2}{2}+\frac{\epsilon_{s2}\rho_s (R_2^2-R_1^2)}{2}+\cdots+\frac{\epsilon_{sN}\rho_s (R_N^2-R_{N-1}^2)}{2}\right\}$$
$$\rho_s=1.654\text{ g/cm}^3$$
$$R=R_N \quad \text{(A4)}$$

and expressed as:

$$\frac{2}{R_N^2}\left\{\frac{0.00746\times 1.654\times 3.115^2}{2}+\frac{0.02424\times 1.654\times(R_N^2-3.115^2)}{2}\right\}$$
$$=0.00746\times 1.654\text{ g/cm}^3 \text{ for } R_N\le 3.115 \quad \text{(A5)}$$

for this example. Axial acceleration is depicted by:

$$\frac{2}{R^2}\int_0^R \frac{\partial(\epsilon_s \rho_s V_s^2)}{\partial z}\, rdr \quad \text{(A6)}$$

Similarly as with the weight of the bed this integral is approximated as:

$$\frac{2}{R_N^2}\left\{\frac{\partial(\epsilon_{s1}\rho_s V_{s1})}{\partial z}\frac{R_1^2}{2}+\frac{\partial(\epsilon_{s2}\rho_s V_{s2}^2)}{\partial z}\frac{(R_2^2-R_1^2)}{2}+\cdots+\frac{\partial(\epsilon_{sN}\rho_s V_{sN}^2)}{\partial z}\frac{(R_N^2-R_{N-1}^2)}{2}\right\} \quad \text{(A7)}$$

due to the incremental means by which the data was obtained. The axial acceleration gradient was approximated with the data obtained at the riser heights of 4.18 and 5.52 m. This term was approximated as:

$$\frac{\partial(\epsilon_s \rho_s V_s^2)}{\partial z}=\frac{(F_s V_s)|_{h=5.52M}-(F_s V_s)|_{h=4.18\ M}}{5.52M-4.18M} \quad \text{(A8)}$$
$$\text{Flux}=F_s=\epsilon_s \rho_s V_s$$

Radial riser velocity profiles were numerically approximated with a least-squares interpolating polynomial that varied from 5th to 8th degree. The shear rate is taken as the derivative of

Table A1. Sample of Data Analysis

Radial Position (cm)	Shear Rate (1/s)	Viscosity (cp)	Shear Stress (Pa)	Axial Pres. Gradient (kg/m^3)	Wt. of Bed (kg/m^3)	Acceleration (kg/m^3)
3.75	−1,511	0.45	−0.68	20.35	20.94	3.10
3.56	−758	0.44	−0.33	20.35	18.84	3.42
3.43	−401	0.23	−0.09	20.35	17.24	3.67
2.93	279	2.02	0.56	20.35	12.34	4.09
2.80	330	1.73	0.57	20.35	12.34	3.84
2.67	354	1.65	0.58	20.35	12.34	3.55
2.54	358	1.67	0.60	20.35	12.34	3.22
2.42	348	1.73	0.60	20.35	12.34	2.92
2.29	329	1.83	0.60	20.35	12.34	2.66
2.16	304	1.97	0.60	20.35	12.34	2.35

the polynomial. For this example, the velocity profile is represented by:

$$V_s = 3.80712 + 0.227102r - 0.274557r^2 + 0.0615718r^3 + 0.0263535r^4 + 0.0198888r^5 - 0.00486317r^6 - 0.00178782r^7 + 0.000250917r^8 \quad \text{(A9)}$$

In Table A1, the weight of the bed, shear rate, shear stress, axial pressure gradient, axial acceleration, viscosity, flux, velocity, and other combined effects are tabulated as a function of the radial position in increments of 0.0635 cm. Note that the viscosity varies only slightly between the radial position of −1.972 cm and −2.988 cm, though the shear rate varies from 240 to 358 s^{-1}. The solid volume fraction has a relatively constant value of 0.00746. In this region, the velocity profile and thus the shear rate are more well defined due to the large velocity variation across this transitional sector between the core and annulus. From this table, the single data point of 1.8 cp for viscosity and a solid volume fraction of 0.00746 is extracted, and similarly 14 other data points are extracted from the 14 additional velocity profiles as plotted in Figure 28. For four of the profiles including this entity, it was necessary to impose a no-slip condition at the wall to get unambiguous results using the method outlined in this study. These profiles were the most dilute cases studied, and from visual observation of the riser, this boundary condition appears to be reasonable for the operating conditions. The data are considered accurate enough for viscosity calculation only in the transition region between the core and annulus. However, note that in the core the axial pressure gradient is greater than the weight of the bed, and the shear rate is positive, yielding as a consequence positive values of viscosity. Similarly, in the annulus where the axial pressure gradient is less than the weight of the bed, the shear rate is negative, thus also yielding positive values of viscosity.

Manuscript received Dec. 3, 1991, and revision received June 16, 1992.